iScience

CellPress
OPEN ACCESS

Article

Mesoporous manganese nanocarrier target delivery metformin for the co-activation STING pathway to overcome immunotherapy resistance

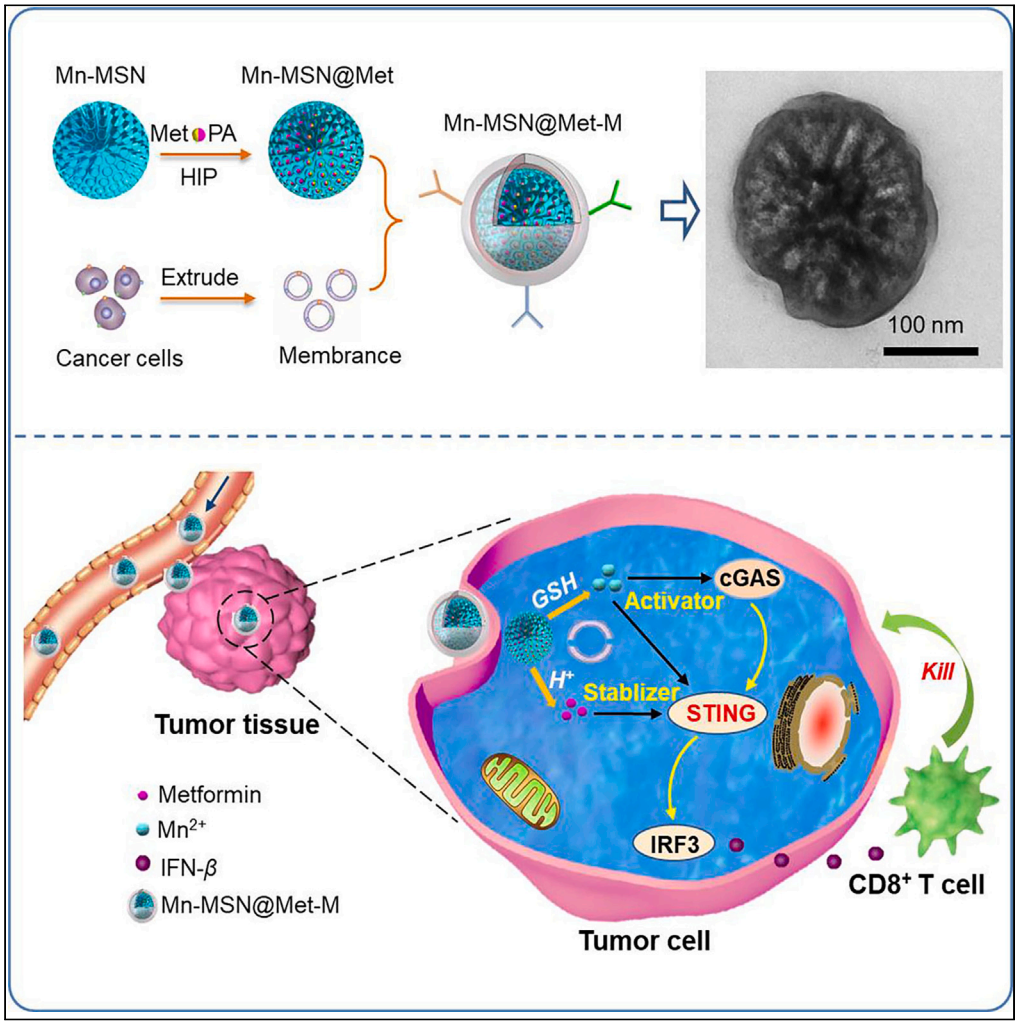

Yuanyao Dou, Jie Zheng, Jun Kang, ..., Li Li, Liling Tang, Yong He

tangliling@cqu.edu.cn (L.T.)
heyong@tmmu.edu.cn (Y.H.)

Highlights

We constructed multifunctional anti-resistance Mn-MSN@Met-M nanoparticles

The NPs can actively target tumor and respond to release Mn^{2+} and metformin

The synergistic activated STING pathway by Mn^{2+} and metformin elevates IFN-β

Mn-MSN@Met-M NPs enhanced the antitumor effect of a PD-1 inhibitor

Dou et al., iScience 27, 110150
July 19, 2024
https://doi.org/10.1016/j.isci.2024.110150

iScience

CellPress
OPEN ACCESS

Article

Mesoporous manganese nanocarrier target delivery metformin for the co-activation STING pathway to overcome immunotherapy resistance

Yuanyao Dou,[1,2,5] Jie Zheng,[2,3,5] Jun Kang,[2,5] Liping Wang,[4,5] Daijuan Huang,[2,3] Yihui Liu,[2] Chao He,[2] Caiyu Lin,[2] Conghua Lu,[2] Di Wu,[2] Rui Han,[2] Li Li,[2] Liling Tang,[1,*] and Yong He[2,3,6,*]

SUMMARY

Targeting the stimulator of interferon genes (STING) pathway is a promising strategy to overcome primary resistance to immune checkpoint inhibitors in non-small cell lung cancer with the STK11 mutation. We previously found metformin enhances the STING pathway and thus promotes immune response. However, its low concentration in tumors limits its clinical use. Here, we constructed high-mesoporous Mn-based nanocarrier loading metformin nanoparticles (Mn-MSN@Met-M NPs) that actively target tumors and respond to release higher concentration of Mn^{2+} ions and metformin. The NPs significantly enhanced the T cells to kill lung cancer cells with the STK11 mutant. The mechanism shows that enhanced STING pathway activation promotes STING, TBKI, and IRF3 phosphorylation through Mn^{2+} ions and metformin release from NPs, thus boosting type I interferon production. *In vivo*, NPs in combination with a PD-1 inhibitor effectively decreased tumor growth. Collectively, we developed a Mn-MSN@Met-M nanoactivator to intensify immune activation for potential cancer immunotherapy.

INTRODUCTION

Lung cancer has the highest mortality rate among all cancers, causing 1.8 million deaths per year.[1] In recent years, immune checkpoint inhibitors (ICIs), represented by programmed death-1 (PD-1)/programmed death-ligand-1 (PD-L1) inhibitors, have demonstrated promising activity in non-small cell lung cancer (NSCLC). However, only 15–25% of patients benefit from ICIs, and most patients with advanced NSCLC develop primary resistance.[2] Mutations in STK11 (LKB1), a tumor suppressor gene encoding serine/threonine kinase,[3] are a major cause of primary resistance to ICIs in NSCLC.[4] The mechanism demonstrated that LKB1 loss leads to the suppression of stimulator of interferon genes (STING) expression,[4,5] which failed to trigger type I interferon (IFN) production and consequently facilitated immune escape.[6] Therefore, restoring STING expression is a promising strategy to overcome the primary resistance of ICIs in NSCLC with the STK11 mutant.

Metformin, a classic oral anti-hyperglycemic agent for type II diabetes mellitus, has anticancer effects for treating melanoma, lung, pancreatic, colon and rectal cancers.[7–10] Previous research has shown that metformin can act as an essential regulator of T cell antitumor immunity by reprogramming metabolism,[11] relieve hypoxia,[12] increase the proportion of $CD8^+$ T cells,[8] and prevent immunologic exhaustion of $CD8^+$ lymphocytes,[7] leading to improved effectiveness of anti-PD-1 therapy. Ren's research revealed that metformin can induce STING expression and activate the STING/IRF3/IFN-β pathway in pancreatic cancer.[10] Recently, our research demonstrated that metformin combined with a PD-1 inhibitor enhanced the antitumor efficacy against STK11-mutant lung cancer through AXIN-1-dependent inhibition of STING ubiquitination.[13] In addition, clinical cases showed that metformin combined with a PD-1 inhibitor had a significant effect on tumor treatment.[8,14] However, retrospective clinical studies have further reported that patients treated with metformin plus atezolizumab did not significantly improve outcomes,[15] which may be due to the insufficient dose of metformin in the tumor.[16] Reportedly, the antitumor effect of metformin is significantly dose-dependent, and the anticancer effect is noticeable only at high doses of 10–30 mM.[17] It is difficult to rally administer such a large dose of metformin to patients. Therefore, finding a way to increase the local concentration of metformin in tumors is the key to enhancing immunotherapy.

Manganese (Mn) is an essential trace element for human health and plays an important role in antitumor immune responses. Recently, it was discovered that Mn^{2+} ions directly activated the cGAS-STING pathway and improved the efficacy of clinical immunotherapy.[18,19] Mn-insufficient mice had significantly enhanced tumor growth and metastasis, with considerably reduced tumor-infiltrating $CD8^+$ T cells.

[1]Key Laboratory of Biorheological Science and Technology, Ministry of Education, College of Bioengineering, Chongqing University, Chongqing 400044, China
[2]Department of Respiratory Disease, Daping Hospital, Army Medical University, Chongqing 400042, China
[3]School of Medicine, Chongqing University, Chongqing 400044, China
[4]Department of pain treatment, the seventh people's Hospital of Chongqing, Chongqing 401320, China
[5]These authors contributed equally
[6]Lead contact
*Correspondence: tangliling@cqu.edu.cn (L.T.), heyong@tmmu.edu.cn (Y.H.)
https://doi.org/10.1016/j.isci.2024.110150

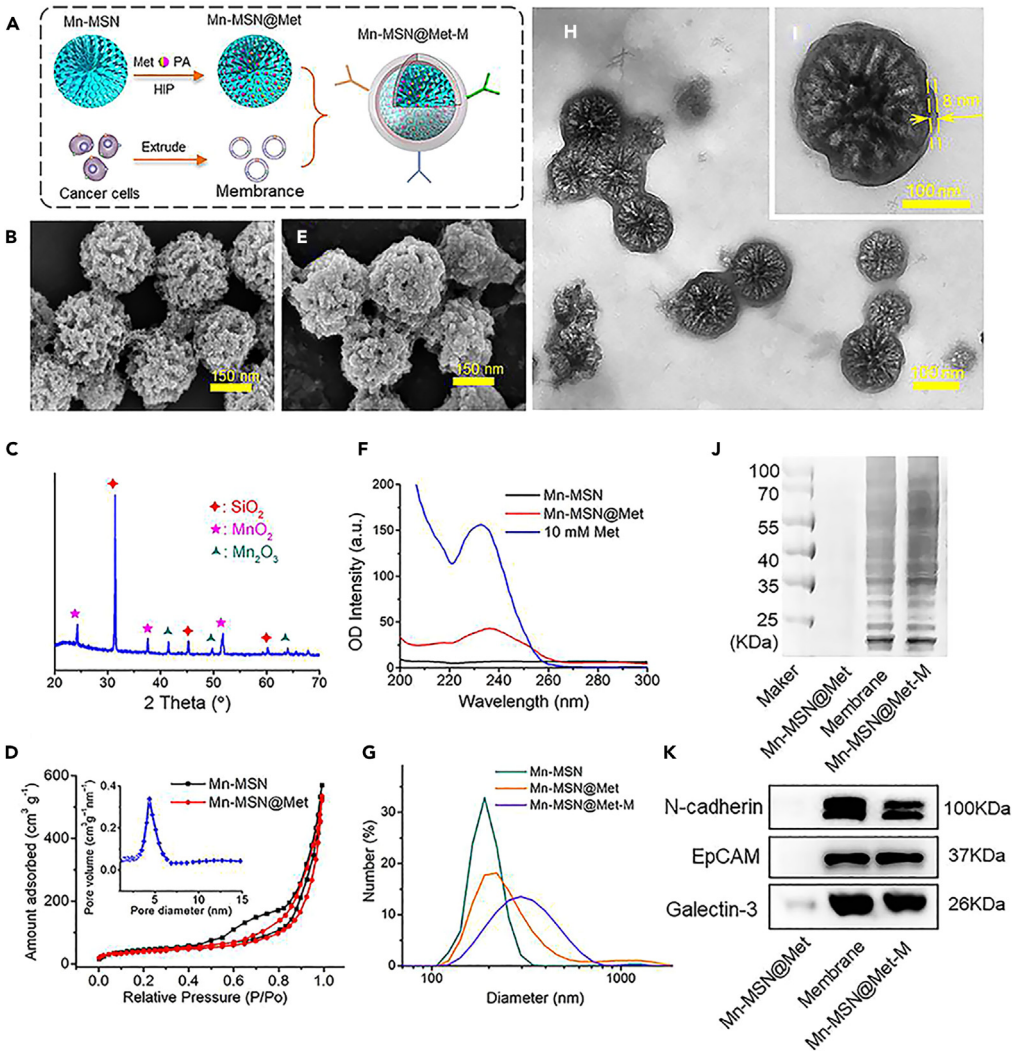

Figure 1. Synthesis and characterization of Mn-MSN@Met-M

(A) Schematic illustration for the synthesis of Mn-MSN@Met-M NPs.

(B) SEM images of Mn-MSN NPs.

(C) XRD patterns of Mn-MSN NPs.

(D) N_2 absorption-desorption isotherms and pore-size distribution curve of the Mn-MSN and Mn-MSN@Met NPs.

(E) SEM images of Mn-MSN@Met NPs.

(F) UV-vis absorption spectra of free metformin, Mn-MSN and Mn-MSN@Met NPs.

(G) Size distribution of Mn-MSN, Mn-MSN@Met and Mn-MSN@Met-M NPs.

(H and I) TEM images of Mn-MSN@Met-M NPs.

(J) Membrane protein by SDS-PAGE of cancer cell membrane vesicle, Mn-MSN@Met and Mn-MSN@Met-M NPs.

(K) Western blotting analysis of specific homologous-binding adhesion molecules on the Mn-MSN@Met-M NPs.

Additionally, exogenous Mn^{2+} significantly increased the IFN-γ and TNF-α level produced by $CD8^+$ T cells,[20] as well as enhanced tumor immune responses to anti-PD-L1 monoclonal antibodies by activating the STING pathway.[21] However, direct administration of Mn^{2+} ions *in vivo* resulted in insufficient accumulation of Mn^{2+} ions in the tumor microenvironment and diffusion of Mn^{2+} ions into other tissues, leading to potential toxicity.[22]

Nanotechnology has provided alternative approaches to address the above challenges through the design of nano-drug delivery systems. Herein, a Mn-based nanocarrier was designed to deliver metformin drug, i.e., Mn-MSN@Met-M NPs (Figure 1A), which can increase the local Mn^{2+} ion and metformin concentrations and promote STING activation (Scheme 1). The synergistically activated cGAS-STING signal pathway by Mn^{2+} plus metformin could elevate cytokine production and T cell recruitment factors to activate $CD8^+$ T cells, which further elicited robust anticancer immune responses to ICIs in STK11-mutant lung cancer.

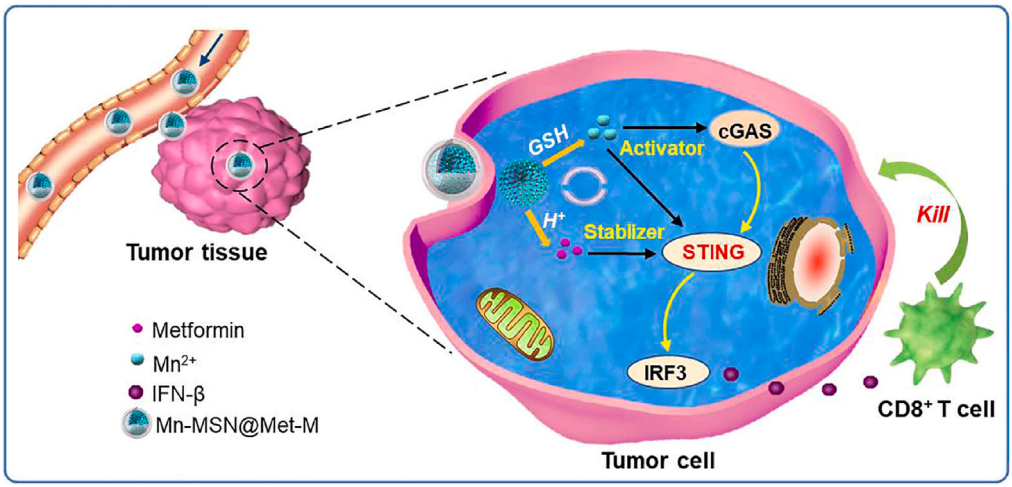

Scheme 1. Mn-MSN@Met-M NPs increase the local Mn^{2+} ion and metformin concentration; further promote the activation of STING

The synergistic activated cGAS-STING signal pathway by Mn^{2+} plus metformin could elevate the IFN-β cytokines production and T cell recruitment factors to activate $CD8^+$ T cells, which further elicit robust anticancer immune responses to ICIs in STK11 mutant lung cancer.

RESULTS

Design, synthesis, and characterization of Mn-MSN@Met-M NPs

The procedure for the synthesis of Mn-MSN@Met-M NPs includes four steps (Figure 1A): (1) Manganese-doped mesoporous silica nanoparticles (Mn-MSNs) with a mesoporous structure were synthesized by an *in-situ* topological process. (2) We used pamoic acid (PA) as an *in situ* hydrophobic ion trapping agent (HIP) for metformin drug loading in the mesoporous of the Mn-MSNs.[23] (3) Cancer cell membranes were collected by freezing and thawing cancer cells from human tumor tissue following the literature protocol.[24] (4) Mn-MSN@Met NPs were coated with membranes through physical extrusion facilitates.[25]

Scanning electron microscope (SEM) and transmission electron microscope (TEM) images of Mn-MSN NPs clearly revealed a spherical morphology with abundant mesoporous structure (Figures 1B and S1A). X-ray diffraction (XRD) pattern (Figure 1C) of the Mn-MSNs revealed several broadened peaks of Mnx(SiO4)y that can be indexed to a braunite-1Q (JCPDS No.33-0904) phase,[26] which illustrates a considerable quantity of doped Mn in the MSN framework. Energy dispersive X-ray spectroscopy (EDX) elemental mapping clearly demonstrated the presence of Mn, O, and Si ions in the whole matrix of Mn-MSN NPs (Figure S1B). Inductively coupled plasma atomic emission spectrometry (ICP-AES) analysis revealed that the Mn-doping amount was approximately 12.4% (*w/w*) in the MSN NPs. Nitrogen adsorption-desorption experiments showed that the Mn-MSNs had a Brunauer-Emmett-Teller (BET) surface area of 326.4 m^2/g and a median pore size of 4.8 nm (Figure 1D), which provided a favorable condition for metformin loading.

The Mn-MSN@Met NPs were synthesized by a novel *in situ* HIP-based active loading technique. The SEM and TEM images (Figures 1E and S1C) of Mn-MSN@Met NPs clearly revealed that the mesoporous structure of the NPs decreased significantly after loading the metformin drug. BET measurements (Figure 1D) further confirmed that the BET surface area of the Mn-MSN@Met NPs was approximately 126.7 m^2/g. Ultraviolet-visible (UV-vis) spectroscopy was used to check metformin loading, and the spectrum revealed that the obtained Mn-MSN@Met NPs showed a characteristic absorbance for metformin at 237 nm (Figure 1F).The Met-loading amount calculated from the absorbance was approximately 1.0 mM/g in Mn-MSN@Met NPs.

Subsequently, the Mn-MSN@Met NPs were coated with cancer cell membranes. Dynamic light scattering demonstrated that after the coating process, the diameter of the Mn-MSN@Met NPs increased by approximately 50 nm (Figure 1G), and the zeta potential was approximately equivalent to that of the membrane vesicles (Figure S2A). The TEM images further revealed a nanoparticle core of approx. 160 nm in diameter and a lipid layer shell of approximately 8 nm in thickness (Figures 1H and 1I). The thickness of the lipid shell was consistent with the reported 5–10 nm range,[27] suggesting successful membrane coating on the Mn-MSN@Met NPs. Furthermore, it can be determined that the encapsulation rate of nanoparticles coated by cell membrane is about 80% based on the TEM images (Figure S2B). The protein composition of the Mn-MSN@Met-M NPs was analyzed by performing sodium dodecyl sulfate-polyacrylamide gel electrophoresis (SDS-PAGE) and western blot. As illustrated in Figure 1J, the protein profile of the Mn-MSN@Met NPs was similar to that of the cancer cell membrane vesicles, indicating the membrane protein was reserved on the surface of Mn-MSN@Met-M NPs. Reportedly, cell adhesion is mainly mediated by cellular adhesion molecules (EpCAM, galectin-3, and N-cadherin) on cancer cell membranes.[28] Western blot analysis (Figure 1K) revealed obvious enrichment of these adhesion molecules on Mn-MSN@Met-M NPs, which confirmed that specific homologous binding adhesion molecules were successfully transferred to the shell of the Mn-MSN@Met NPs. Thus, it was suggested that Mn-MSN@Met-M NPs have the potential to maintain specific recognition and binding between the Mn-MSN@Met-M NPs and cancer cells via a homologous binding mechanism.

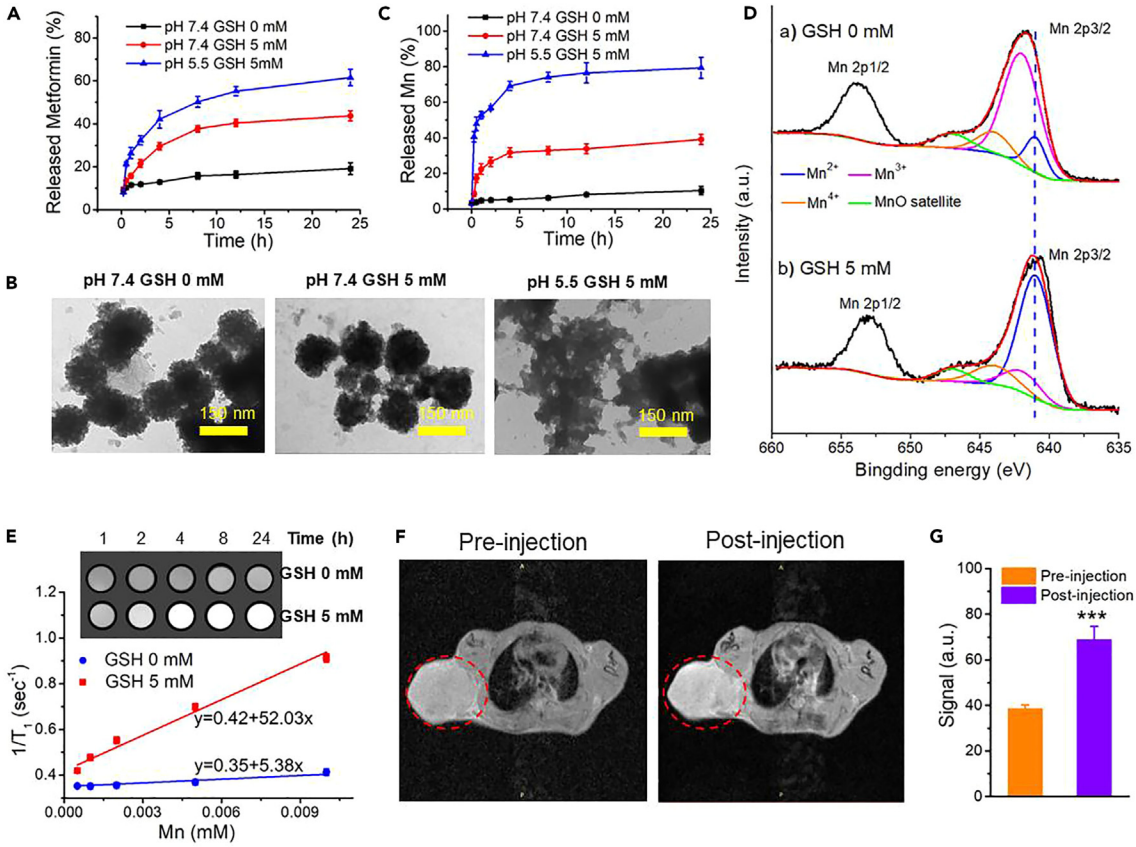

Figure 2. Metformin and Mn ions release profile, and theranostic functions of Mn-MSN@Met-M NPs under tumor microenvironment

(A) Metformin drug release profiles of Mn-MSN@Met-M with different pH (7.4 and 5.5) and GSH (0 mM and 5 mM).

(B) TEM images of the Mn-MSN@Met-M NPs after degradation under tumor microenvironment.

(C) Mn ions release profiles of Mn-MSN@Met-M with different pH (7.4 and 5.5) and GSH (0 mM and 5 mM).

(D) XPS spectra of Mn element under reduce microenvironment.

(E) T1-weighted MR images of the supernatants obtained from Mn-MSN@Met-M NPs in FBS solution at different GSH (0 mM and 5 mM), and the *r*1 values from T1-weighted MR images of Mn-MSN@Met-M NPs incubated in above condition.

(F) MR imaging capability of Mn-MSN@Met-M *in vivo* with H460 tumor-bearing mice at 4 h after tail vein injection.

(G) Signal intensity of tumor area (red circle in F) before and after tail vein injected Mn-MSN@Met-M NPs. Data are represented as mean ± SD ($n = 3$), ***p: <0.001 (compared with pre-injection).

Additionally, the long-term stability of Mn-MSN@Met-M NPs at 37°C in 5% serum (pH: 7.4 and GSH absence) can be estimated by assessing the nanoparticle size fluctuation (Figure S2C). The average size of Mn-MSN@Met-M NPs fluctuated in a small range within 7 days, indicating no obvious aggregation. The hemocompatibility was further investigated to evaluate the safety of the Mn-MSN@Met-M NPs as a nanoagent. The hemolysis ratios of the red blood cells (RBCs) for all concentrations of Mn-MSN@Met-M NPs were negligible compared to the positive control group (H_2O with RBCs) (Figure S2D). The results proved that the Mn-MSN@Met-M NPs had excellent hemocompatibility.

The release profile of metformin and Mn ions and theranostic functions of the Mn-MSN@Met-M NPs under tumor microenvironment

To imitate the tumor microenvironment, simulated body fluid (SBF) solutions with varied pHs and GSH concentrations were adopted for detailed biodegradation evaluations. The metformin release profiles from Mn-MSN@Met-M NPs at two different pHs (7.4 and 5.5) in a reducing microenvironment were investigated (Figure 2A). Under physiological conditions (pH 7.4), only about 18% of metformin was released from the Mn-MSN@Met-M NPs at 24 h, whereas the cumulative release of metformin reached 60% under an acidic tumor microenvironment condition (pH 5.5) with a reducing microenvironment (GSH: 5 mM) at the same time point, which should be caused by the break-up of the composite inorganic nanosystem and subsequent biodegradation to promote fast metformin release.[26] It has been well-demonstrated that Mn-O bonds are sensitive to mildly acidic and reducing microenvironments that cause nano-framework degradation and enable Mn extraction.[26,29] Therefore, the degradation process and Mn ion release profile of the Mn-MSN@Met-M NPs were

monitored via TEM observations and ICP tests under a simulated tumor microenvironment, respectively. The NPs showed no significant change in physiological condition after 24 h, and only partial degradation even under reducing conditions (pH 7.4, GSH 5 mM) (Figure 2B). Surprisingly, the Mn-MSN@Met-M NPs exhibited remarkable degradation behavior at pH 5.5 with GSH 5 mM solution (Figure 2B). The release of Mn ions from Mn-MSN@Met-M was substantially accelerated under mildly acidic conditions compared to that in neutral SBF (Figure 2C). Similar to the influence of pH, the presence of GSH also accelerated the release of Mn from the carrier. The Mn-release rates under such a combinatorial condition were much higher than the biodegradation rate in either acidic or reducing condition, and its maximum release rate was 80%. X-ray photoelectron spectroscopy (XPS) was utilized to analyze the valence state of the Mn element under acidic and reducing conditions. The main peak of Mn 2p3/2 could be divided into three characteristic peaks at 641, 642, and 644 eV, which were indexed to the Mn^{2+}, Mn^{3+}, and Mn^{4+} species,[30] respectively (Figure 2D). Compared with the untreated GSH, the Mn^{2+} content was significantly increased under reducing conditions, which could be interpreted as Mn^{3+} and Mn^{4+} species reduced to Mn^{2+} by GSH.

As Mn^{2+} with five unpaired 3d electrons has been demonstrated to be an effective T_1-MR contrast agent,[31] the T_1 contrast-enhanced magnetic resonance imaging (MRI) capability of Mn-MSN@Met-M NPs was evaluated under acidic and reducing conditions using a clinical 3.0 T human clinical scanner, and the effect of MRI *in vitro* is summarized in Figure 2E. A significant concentration-dependent brightening effect of the Mn-MSN@Met-M NPs sample was observed in the T_1-MR images at 5 mM GSH, whereas the nanoparticle signals in the neutral buffer solution appeared much weaker. Additionally, the initial longitudinal relaxivity r_1 of Mn-MSN@Met-M NPs under reducing conditions was 52.03 $mM^{-1}s^{-1}$, which was much higher than that of the neutral condition samples (GSH = 0 mM is 5.38 $mM^{-1}s^{-1}$) after incubation for 24 h (Figure 2E). Such contrast-enhanced responsiveness can be attributed to the large amount of Mn^{2+} reduced under reducing conditions.

Considering the excellent *in vitro* MR imaging capability of Mn-MSN@Met-M NPs, we further explored their potential as a contrast agent for *in vivo* MRI. A mouse bearing a tumor was imaged using a 3.0 T clinical MR scanner at pre-injection and 4 h after tail vein injection of Mn-MSN@Met-M NPs (Figure 2F). The tumor area of the mouse appeared dark before the injection of the Mn-MSN@Met-M NPs but remarkable brightened at 4 h post-injection (red dashed circles in Figures 2F and 2G). This significant T_1 contrast effect makes Mn-MSN@Met-M NPs ideal as a highly efficient T_1 contrast agent for MRI.

Homologous targeting evaluation, uptake, and lysosomal escape *in vitro*

Prior to performing the homologous targeting capability studies, we assessed the biocompatibility of Mn-MSN@Met-M NPs *in vitro* using H460 and LLC cancer cells with the SKT11 mutant. As shown in Figures 3A and 3B, after incubation with Mn-MSN@Met-M NPs for 48 h, both H460 and LLC cells retained more than 90% viability even at high particle concentrations up to 0.2 mg/mL, suggesting good biocompatibility of Mn-MSN@Met-M NPs. Then, H460 cells were incubated with free sulfo-cyanine 5 (Cy5), Cy5-labeled Mn-MSN@Met, Mn-MSN@Met-M_{LLC} (LLC cell membrane coated), and Mn-MSN@Met-M_{H460} (H460 cell membrane coated) for 4 h, followed by fluorescence microscopy imaging and flow cytometry analysis. The cells exhibited bright red fluorescence after incubation with Mn-MSN@Met-M_{H460} and minimal fluorescence when incubated with free Cy5, Cy5-labeled Mn-MSN@Met, or Mn-MSN@Met-M_{LLC} (Figures 3C and 3D), indicating effective binding of Mn-MSN@Met-M_{H460} onto H460 cells. Comparatively, the LLC cells exhibited bright red fluorescence when incubated with Mn-MSN@Met-M_{LLC} NPs (Figures S3A and S3B). These results provide direct evidence of the homologous targeting capability of the cancer membrane-coated NPs.

To detect the cellular uptake behavior, the NPs were labeled with fluorescein isothiocyanate (FITC) fluorescence and observed using confocal laser scanning microscopy. The human lung cancer H460 cells were incubated with free FITC and FITC-labeled Mn-MSN@Met-M_{H460} NPs for 4 h. As presented in Figure 3E, an excellent strong green fluorescence signal from Mn-MSN@Met-M_{H460} NPs was observed from within the cytoplasm of the H460 cells compared with the control group, indicating that the Mn-MSN@Met-M_{H460} NPs significantly enhanced translocation of drugs into cells through the endocytosis process. Additionally, the passage of NPs from lysosomes into the cytoplasm is considered a critical step for drug delivery because the enzymes in the lysosomes will inactivate with the drugs. Lysosomes are membrane bound organelles with an internal pH of about 5.5.[32] Under acidic conditions, the membrane on NPs will crack and fuse with the lysosome membrane, resulting in lysosome rupture.[33] After 8 h of uptake, the overlapping green fluorescence and lysosomal red fluorescence of the control group suggested that most free FITC molecules were captured in lysosomes. In contrast, the apparent separation of green fluorescence and lysosomal red fluorescence indicated successful lysosomal escape of the Mn-MSN@Met-M_{H460} NP group (Figure 3E).

Mn-MSN@Met-M NPs enhanced T cell-mediated killing of lung cancer cells *in vitro*

We have previously reported that metformin can enhance T cell-mediated killing of lung cancer cells *in vitro*.[13] We also determined whether Mn-MSN@Met-M NPs can reinforce T cell killing of H460 and LLC cells. The different proportions of T cells and H460 cells treated with free metformin, Mn-MSN-M, and Mn-MSN@Met-M NPs, then the viability of H460 cells were measured by the CCK-8 assay. Both free metformin and Mn-MSN-M NPs could enhance the killing of H460 cells by T cells (Figure 4A). Importantly, the viability of H460 cells was dramatically inhibited when Mn-MSN@Met-M NPs were combined with T cells. Typically, when the ratio of T cells to H460 cells was 1:1, the survival rate of H460 cells was less than 20%, which was much lower than that of the free metformin (50%) and Mn-MSN-M NPs (60%) groups (Figure 4B). Similarly, Mn-MSN@Met-M NPs can significantly enhance the killing effect of T cells on LLC cells (Figures 4C and 4D). The effect of Mn-MSN@Met-M NPs on T cell-mediated killing of H460 and LLC cells has been elucidated through the colony formation assay. As shown in Figures 4E and 4F, free metformin, Mn-MSN-M, or Mn-MSN@Met-M NPs alone showed exerted minimal effect on colony formation of

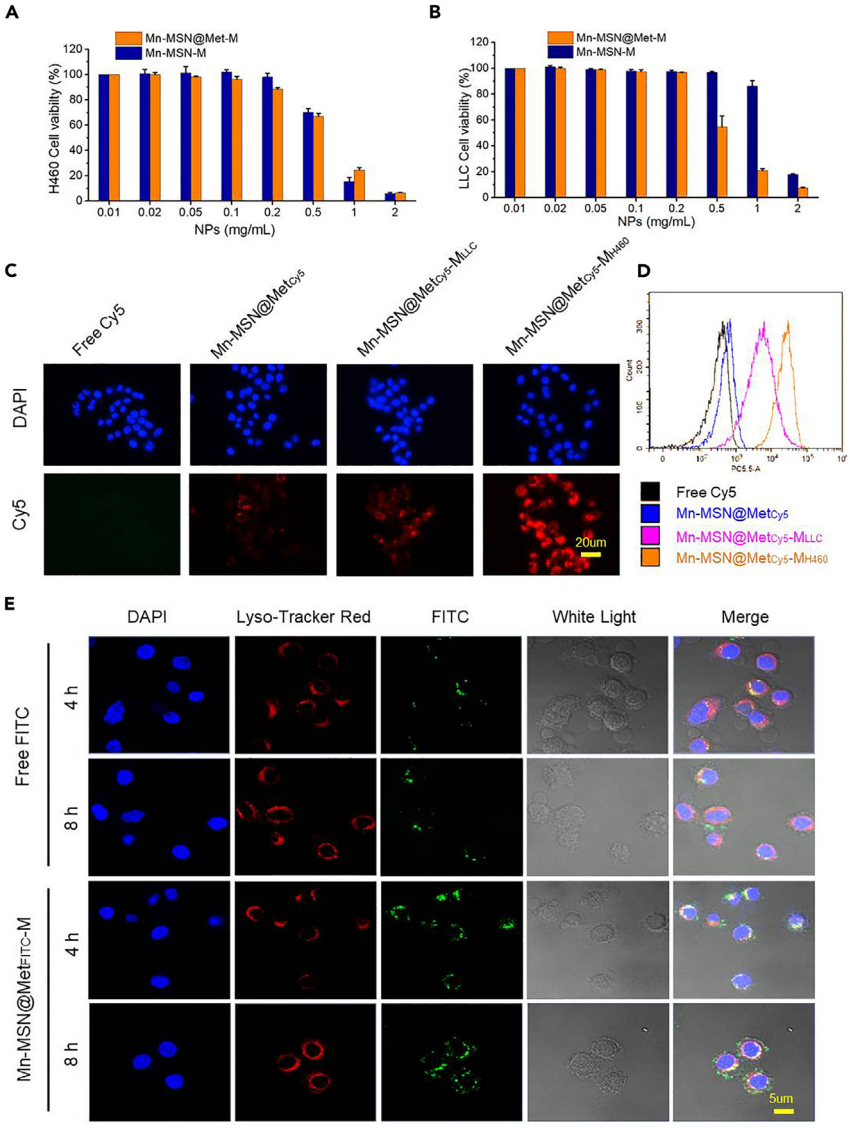

Figure 3. Homologous targeting evaluation, uptake, and lysosomal escape in *vitro*

(A and B) *In vitro* cell toxicity in H460 and LLC cells of Mn-MSN@Met and Mn-MSN@Met-M NPs. Homologous targeting evaluation, (C) fluorescence images and (D) flow cytometry analysis of H460 cancer cells after incubation with free Cy5, Cy5-labeled Mn-MSN@Met and Cy5-labeled Mn-MSN@Met coated by membrane of H460 and LLC, respectively.

(E) Cellular uptake and lysosome escape of Cy5-labeled Mn-MSN@Met-M_{H460}. Confocal microscopy observed the H460 cellular uptake of free Cy5 and Cy5-labeled Mn-MSN@Met-M_{H460} at a concentration of 100 μg/mL.

H460 and LLC cells, whereas the combination with activated T cells (1:1 ratio of T cells to cancer cells) significantly decreased cancer cell growth, especially in the Mn-MSN@Met-M NPs group. Taken together, these results suggest that Mn-MSN@Met-M NPs enhanced T cell-mediated killing of lung cancer cells *in vitro*.

In our previous research, we found that metformin enhanced the stabilization of STING and led to the activation of its downstream signaling pathway.[13] Recently, multiple studies have discovered that Mn^{2+} ions can directly activate the cGAS-STING pathway and improve the efficacy of antitumor immunity.[21,22,34] In this work, we speculated that the cGAS-STING pathway was synergistically activated by metformin and Mn^{2+} released from the Mn-MSN@Met-M NPs. To confirm the activation of the cGAS/STING pathway, the expression level of STING/phosphorylated STING (p-STING), and its downstream markers TBK1/phosphorylated TBK1 (*p*-TBK1) and IRF3/phosphorylated IRF3 (*p*-IRF3) were determined by western blot (Figures 4G and 4H). It was found that STING was almost hardly regulated, but p-STING was augmented in metformin and Mn-MSN-M NP groups, especially in Mn-MSN@Met-M NPs, confirming that metformin plus Mn^{2+} could cause much stronger STING phosphorylation. Furthermore, TBK1 and IRF3 phosphorylation dependent upon the integrity of the cGAS/STING pathway were also

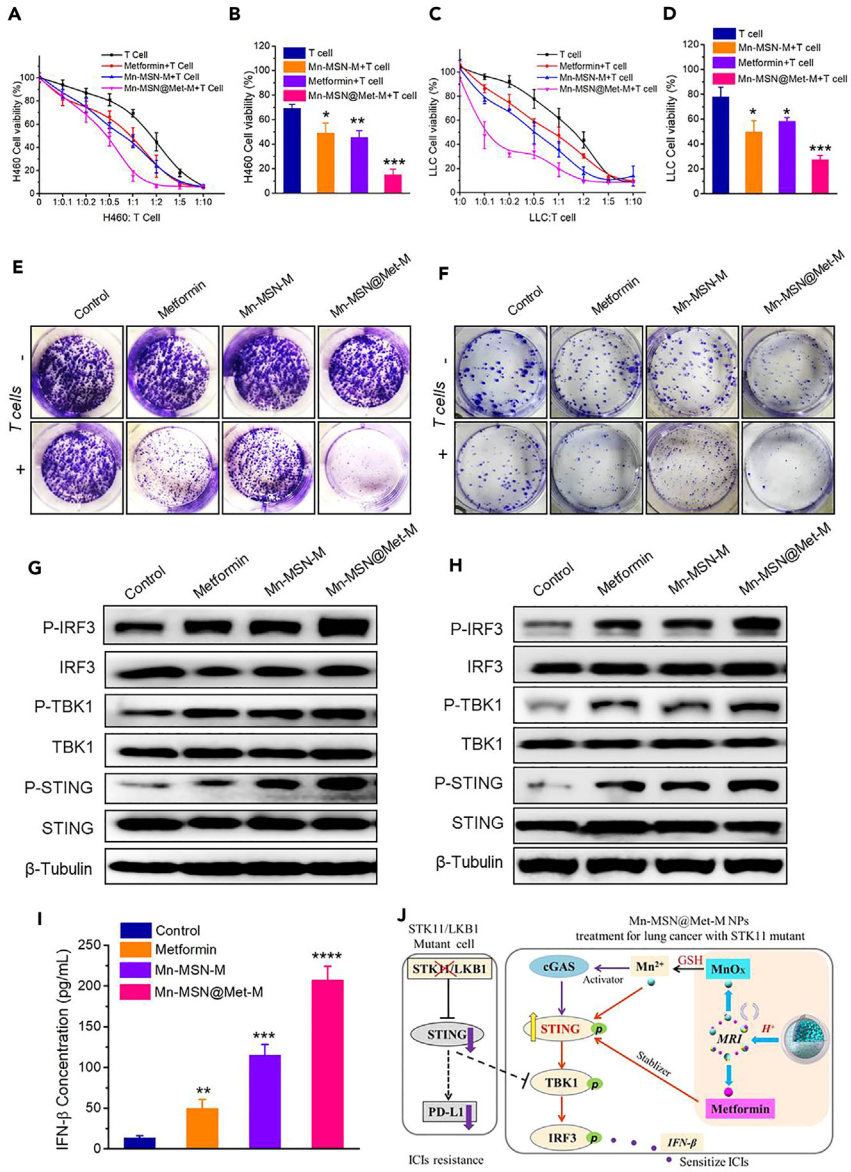

Figure 4. Mn-MSN@Met-M NPs enhanced T cell-mediated killing of lung cancer cells in *vitro*

(A and C) The viability of H460 (or LLC) cells was measured by CCK-8 assay at different proportions of T cell and H460 (or LLC) cell treated with free metformin, Mn-MSN-M, and Mn-MSN@Met-M NPs; (B, D) The viability of H460 (or LLC) cells at 1:1 proportion of T cell and H460 cell, data are represented as mean ± SD ($n = 3$) *: $p < 0.05$, **: $p < 0.01$, ***: $p < 0.001$ (compared with T cell).

(E and F) Representative images of the colony formation ability of H460 (or LLC) cells at 1:1 proportion of T cell and H460 (or LLC) cell treated with free metformin, Mn-MSN-M, and Mn-MSN@Met-M NPs at a concentration of 100 μg/mL.

(G and H) The STING, TBK1, IRF3 and phosphorylation STING, TBK1, IRF3 proteins were measured by western blot assay combined treated with free metformin, Mn-MSN-M, and Mn-MSN@Met-M NPs in H460 and LLC cells. β-Tubulin was used to confirm equal gel loading.

(I) Cytokine concentration of IFN-β secreted by H460 cells after treated with free metformin, Mn-MSN-M, and Mn-MSN@Met-M NPs, data are represented as mean ± SD ($n = 3$), *: $p < 0.05$, **: $p < 0.01$, ***: $p < 0.001$, ****: $p < 0.0001$ (compared with Control).

(J) Schematic diagram of cGAS-STING signaling pathway activated by Mn-MSN@Met-M NPs.

observed to be dramatically upregulated in Mn-MSN@Met-M NPs, compared with other groups, demonstrating the cGAS/STING signal pathway was synergistically activated by Mn-MSN@Met-M NPs (Figure 4J). Reportedly, the activation of the IRF3 pathway induced the secretion of type I IFNs, such as IFN-β.[22] Thus, we further determined IFN-β production in the H460 cell line using the enzyme-linked immunosorbent assay (ELISA). Mn-MSN@Met-M NPs triggered the highest secretion of IFN-β among all other control groups, which should further promote T cells antitumor immune responses (Figure 4I).

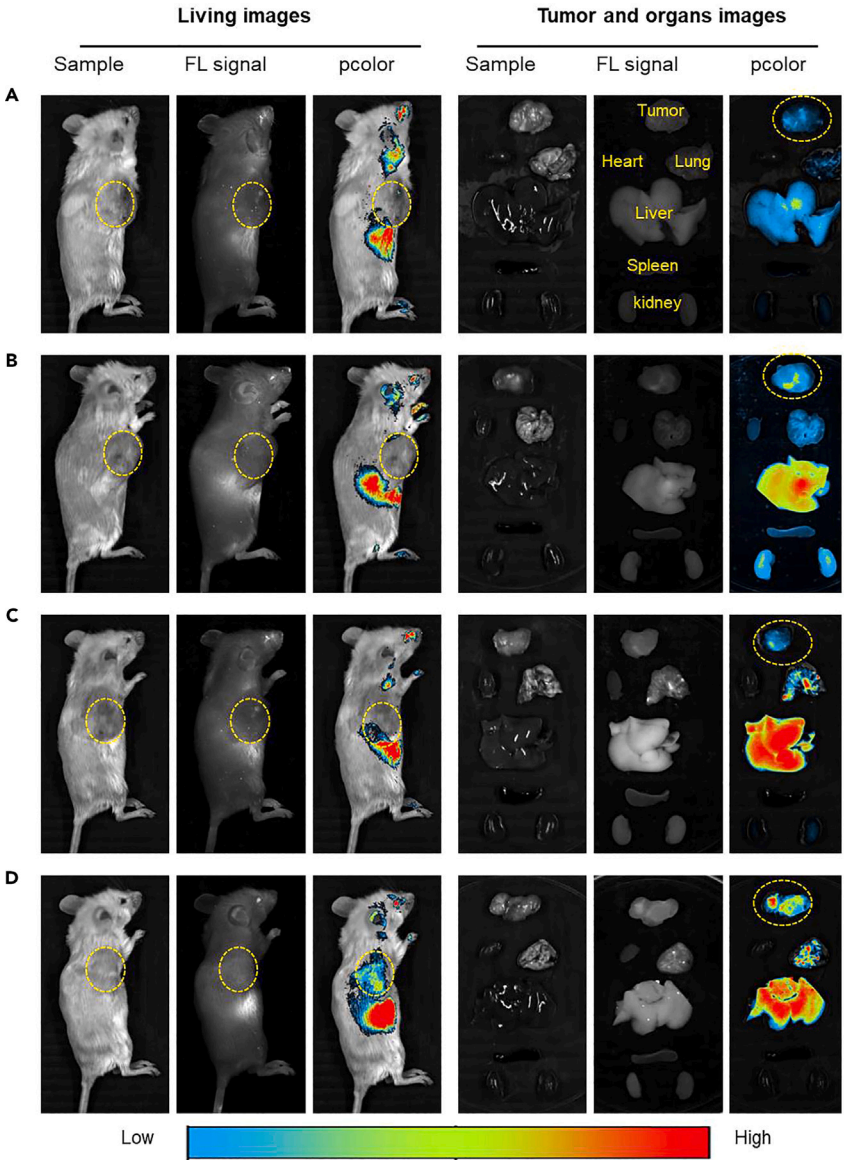

Figure 5. The tumor-targeting effect of Mn-MSN@Met-M NPs *in vivo*

The whole body distribution of free Cy5, Cy5-labeled Mn-MSN@Met and Mn-MSN@Met-M NPs was determined by *in vivo* imaging system.
(A) Control (PBS), (B) Free Cy5, (C) Mn-MSN@MetCy5, (D) Mn-MSN@MetCy5-M. **Left**: *In vivo* imaging of mice. **Right**: the tumors and major organs of sacrificed mice were collected for the ex *vivo* imaging.

Tumor-targeting effect of Mn-MSN@Met-M NPs *in vivo*

Prior to performing the antitumor capability studies, we assessed the tumor-targeting effect of NPs *in vivo*; the whole body distributions of free Cy5, Mn-MSN@Met-M, and Cy5-labeled Mn-MSN@Met-M NPs were determined using an *in vivo* imaging system (Figures 5A–5D). Free Cy5, Mn-MSN@Met-M, and Cy5-labeled Mn-MSN@Met-M NPs were delivered by caudal vein injection to NOD-SCID mice, respectively. Selective accumulation in the tumor site faster for H460 membrane coated Mn-MSN@Met NPs than that of the uncoated NPs after injected 8 h (Figures 5C and 5D left), indicating that the cancer cell membrane-coated particles enhanced the active targeting ability, and there are a few Mn-MSN@Met NPs that could accumulate in tumor sites through the EPR effect (Figure 5B left).[35] To further analyze the biodistribution of NPs, the tumors and major organs of sacrificed mice were collected for ex *vivo* imaging. The tumors of the mice treated with Cy5-labeled Mn-MSN@Met-M NPs exhibited the strongest fluorescence signal (Figure 5D right), further confirming the tumor targeting efficacy of Mn-MSN@Met-M NPs. Besides, ex *vivo* imaging of organs showed that Mn-MSN@Met and Mn-MSN@Met-M NPs were observed only in the liver, whereas free Cy5 accumulated in the liver and kidney, demonstrating that the Mn-MSN@Met-M NPs exhibit few side effects in other organs. Subsequently, we further examined the distribution of Mn-MSN@Met-M NPs in major organs and tumors *in vivo* by ICP-AES (Mn ions) and

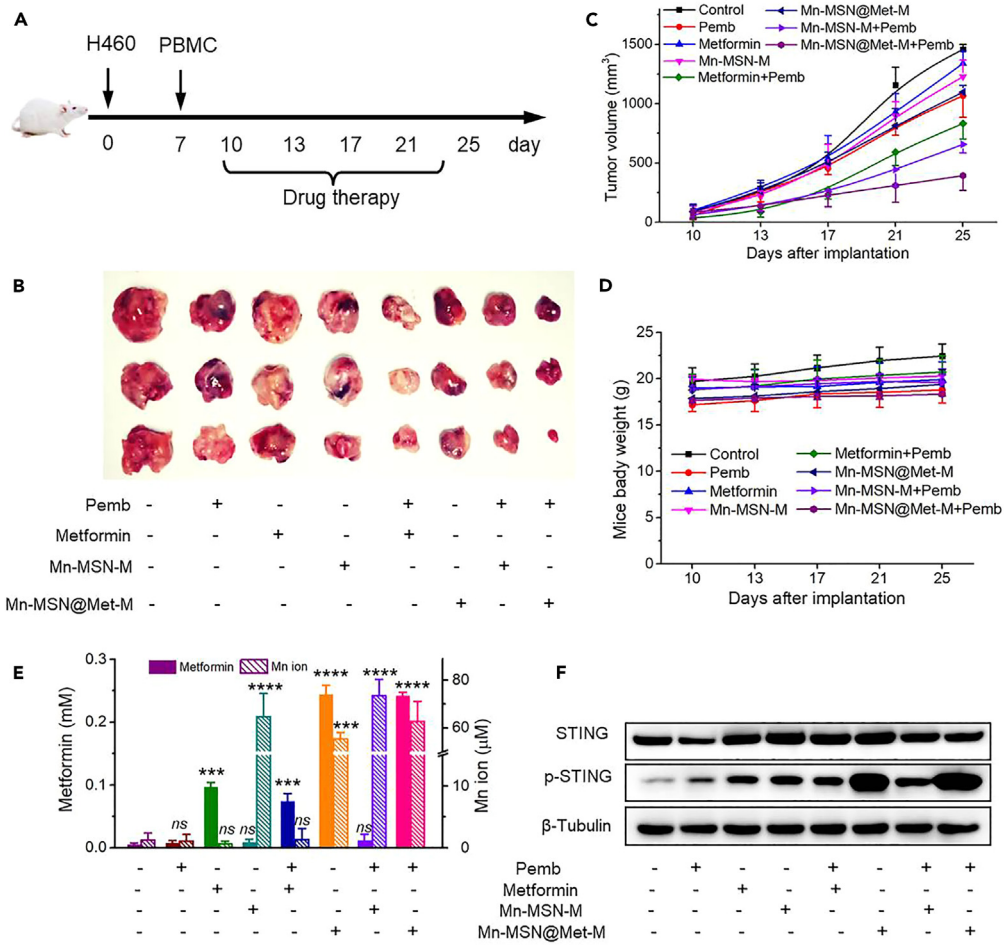

Figure 6. Mn-MSN@Met-M NPs enhanced antitumor efficacy with a PD-1 inhibitor *in vivo*

(A) NOD-SCIDBALB/c mice bearing H460 tumors were treated starting from day 10 with PBS, Pemb antibody, metformin, Mn-MSN-M, Mn-MSN@Met-M, or the combination of antibody and metformin, Mn-MSN-M, Mn-MSN@Met-M.

(B) Representative tumor photographs of H460 tumor-bearing mice at 25th day after indicated treatments.

(C) Tumor growth curves of H460 tumor-bearing mice after intravenous administrations.

(D) Body weight change.

(E) Concentrations of Mn ion and metformin in the tumor site after indicated treatments measurement by ICP-AES and LCMS respectively, data are represented as mean ± SD ($n = 3$), *ns*: no significance, ***: $p < 0.001$, ****: $p < 0.0001$ (compared with Control).

(F) STING activation in tumor model cells by western blot after indicated treatments.

LCMS (metformin) techniques. The results indicated that Mn ion mainly accumulated in tumor sites, with a small amount of accumulation in liver, but no significant accumulation in other organs (Figures S4A and S4B). These results were consistent with those of *in vivo* imaging, suggesting that Mn-MSN@Met-M NPs mainly accumulate into tumors and have less damage to major organs.

Mn-MSN@Met-M NPs enhanced antitumor efficacy with a PD-1 inhibitor *in vivo*

To investigate the effects of combining NPs with a PD-1 inhibitor (Pembrolizumab, Pemb) on tumor growth, we established a PBMCs-CDX mouse model using H460 cells,[36] and treated it with PBS, metformin, Mn-MSN-M, and Mn-MSN@Met-M NPs alone or in combination with Pemb following the schedule shown in Figure 6A. As shown in Figures 6B and 6C, Pemb, metformin, or Mn-MSN-M NPs only slightly inhibited tumor growth. In contrast, the combination of Pemb with metformin or Mn-MSN-M resulted in a significant reduction in tumor volume. Compared with the single drug groups, the Mn-MSN@Met-M NP group showed a notable tumor suppressive effect. Surprisingly, the best tumor suppressive effect was observed from the combination of Pemb and Mn-MSN@Met-M NPs, which had the smallest relative tumor volume at 2 weeks post-injection (Figures 6B and 6C). This result could be attributed to the enhanced tumor accumulation of metformin and Mn ions in the tumor region and the improved the efficacy of Pemb. Meanwhile, the body weights of the tumor-bearing mice were recorded during the tumor therapeutic process (Figure 6D). The body weights of the mice treated with PBS, metformin, Mn-MSN-M,

and Mn-MSN@Met-M NPs alone or in combination with Pemb did not change significantly over the entire treatment period, implying good biosafety of the NPs. In the biosafety assessment, the histology of organs (heart, liver, spleen, lung, and kidneys) and tumors were analyzed at the end of the experiment. H&E staining results show that no morphological differences in major organs (Figure S5), indicating Mn-MSN@Met-M NPs with high biosafety possess potential application in cancer therapy.

To identify the potential mechanism by which the Mn-MSN@Met-M NPs enhanced the efficacy of Pemb, we examined the concentrations of Mn ions and metformin in the tumor site. The concentration of metformin in the tumor was less than 0.1 mM after treatment with free drugs (Figure 6E). Surprisingly, the Mn-MSN@Met-M NPs treatment significantly increased the concentration of metformin at the tumor site (more than three times that of the free drug group). Subsequently, the concentration of Mn ions generated by the Mn-MSN carrier was detected and was as high as 80 μM Mn ions in the group containing Mn-MSN. A recent study with NPs acting as both drug carriers and Mn^{2+} generators demonstrated that Mn^{2+} enhanced cGAS-STING activity.[34] Therefore, western blot was also performed to detect STING activation in tumor model cells (Figure 6F). None of the groups had a significant regulatory effect on total STING protein expression. Encouragingly, p-STING was significantly more activated by Mn-MSN@Met-M NPs compared with Mn-MSN-M or metformin monotherapy, which is consistent with the *in vitro* results. These results indicated that Mn ions and metformin can synergistically activate STING after increasing the concentration of Mn and metformin in tumor sites by Mn-MSN@Met-M NPs, thereby activating its downstream pathway and promoting antitumor immunity.

DISCUSSION

STK11/LKB1 is among the most commonly inactivated tumor suppressors in NSCLC, and its inactivating mutations have been associated with reduced expression of the PD-1 ligand PD-L1 in lung adenocarcinomas.[37] Patients harboring STK11/LKB1 alterations have shorter progression-free and overall survival after anti-PD-1 treatment due to ineffective T cell infiltration.[5,38] STING has emerged as a key regulator of the innate immune response because of the preferential secretion of tumor promoting cytokines/chemokines and type I IFNs and has also become a target for cancer immunotherapy.[39] Activation of the STING pathway promotes the trafficking and infiltration of T cells to tumors, which is crucial for the recognition and killing of cancer cells by T cells.[40]

Recently, multiple studies have discovered that Mn^{2+} ions can directly activate the cGAS-STING pathway and improve the efficacy of antitumor immunity.[18,21,22,41] Our previous work illustrated that metformin can enhance the stabilization of STING.[13] Therefore, we hypothesized that simultaneously increasing the local concentrations of Mn^{2+} ions and metformin at the tumor site could activate and stabilize STING expression. This in turn would synergistically activate the cGAS-STING signaling pathway, providing an effective strategy to enhance the antitumor immunity response. Thus, there has been an urgent need to develop unique strategies to increase the concentrations of Mn^{2+} ions and metformin in the tumor site.

The development of nanotechnology has provided new hope for the enrichment of drugs in tumor sites. A recent promising approach involves designing nanocarriers capable of responsive drug release by utilizing the characteristics of the tumor microenvironment.[42,43] In this study, we developed Mn-MSN@Met-M NPs according to the higher GSH and acidic environment of tumor sites.[26] Under acidic conditions, the framework of Mn-MSN NPs will collapse,[26] and respond to the release of metformin and MnOx triggered by low pH (Scheme 1 and Figure 4J). Subsequently, the MnOx was further reduced to Mn^{2+} by GSH, thus increasing Mn^{2+} content in cancer cells. In our tumor model, the results showed that the concentration of Mn ions and metformin were indeed significantly increased after Mn-MSN@Met-M NP treatment (Figures 6E and 6F). This result is attributed not only to the responsive release of the drug, but also to the specific targeting of the NPs to the tumor cells. Based on the homologous adhesion effect of cancer cell membrane,[44] we coated Mn-MSN@Met NPs with cancer cell membrane to achieve the active targeting function of tumor cells. *In vivo* experiments showed enhanced accumulation of Mn-MSN@Met-M NPs at tumor sites compared to uncoated Mn-MSN@Met NPs (Figures 5C and 5D) because Mn-MSN@Met-M NPs actively target cancer cells after tail vein injection. MRI results further revealed that abundant Mn^{2+} was enriched in the tumor site (Figure 2F). The STING complex is expressed in the endoplasmic reticulum of target cells, so the intracellular delivery of an STING stimulator becomes crucial because it is easily degraded after being captured by lysosomes.[45,46] In this work, we found that Mn-MSN@Met-M NPs were able to escape the capture of lysosomes and enter the cytoplasm smoothly after uptake by cancer cells (Figure 3E). Therefore, we increased the concentration of Mn and metformin drugs at the tumor site by constructing targeted delivery NPs, which are expected to solve the problem of low drug concentrations at the tumor site.

Mn not only plays an important role in regulating innate immune responses,[47] but also acts as an STING agonist. *Jiang* et al. demonstrated that Mn is indispensable for the host defense against cytosolic dsDNA by activating cGAS-STING.[18] Additionally, Mn is essential in the innate immune sensing of tumors and enhances adaptive immune responses against tumors.[19] Combining Mn^{2+} with immune checkpoint inhibition synergistically has been found to boost antitumor efficacies and reduce the anti-PD-1 antibody dosage required in mice. In a previous study, metformin reportedly activated the STING/IRF3/IFN-β pathway and promoted T cell infiltration.[10] Our previous study found that metformin enhances stabilization of STING and the activation of its downstream signaling pathway, which enhances the immune response to PD-1 inhibitors.[13] These results indicate that metformin can be used as a stabilizer for STING. In the current study, we combined an STING agonist and stabilizer to study their effect on activation of the cGAS-STING pathway. The results revealed that STING phosphorylation (p-STING) was remarkably augmented in Mn-MSN@Met-M NPs, which contributed to the enhancing effect of the combination of metformin plus Mn^{2+} on STING stabilization and activation *in vitro* (Figures 4G and 4H). Inspired by this finding, we then analyzed the effect of Mn-MSN@Met-M NPs on the activation of STING by increasing the concentration of Mn ions and metformin in the tumor site (Figure 6G). The result showed that p-STING was significantly activated by Mn-MSN@Met-M NPs compared with Mn-MSN-M or metformin monotherapy. Mechanism exploration

further revealed that TBK1 and IRF3 phosphorylation dependent upon the integrity of the cGAS/STING pathway were also upregulated by Mn-MSN@Met-M NPs (Figures 4G, 4H, and 4J). Furthermore, a higher level of IFN-β was generated after treatment with Mn-MSN@Met-M NPs, which contributed to superior antitumor efficacy (Figure 4I). Metformin plus Mn^{2+} enhanced T cell-mediated killing of lung cancer cells *in vitro*. *In vivo*, the combination of Pemb and Mn-MSN@Met-M NPs showed the best tumor suppressive effect in a PBMC-CDX model. Taken together, these results suggest that a metformin stabilizer plus a Mn^{2+} agonist synergistically enhances PD-1 inhibitor efficacy in STK11 mutant NSCLC by activating STING expression.

In conclusion, in the present study, we proposed the idea of synergistic activation of the STING signaling pathway via the activation effect of Mn on the STING pathway and the stabilization effect of metformin on the STING protein. In order to solve the deficiency of low concentrations of metformin and Mn^{2+} ions in tumor sites, we constructed Mn-MSN@Met-M NPs that can actively target tumors and respond by releasing Mn^{2+} ions and metformin in tumor microenvironments. *In vitro* and *in vivo* experiments confirmed that Mn-MSN@Met-M NPs effectively enhanced the ability of T cells to kill tumor cells and improved the efficacy of PD-1 monoclonal antibodies for the treatment of STK11 mutant lung cancer. In summary, this study offered a coordinated strategy to enhance the STING pathway, holding considerable potential for enhancing the efficacy of ICIs.

Limitations of the study

Our study offers promising insights to overcome primary resistance to ICIs in NSCLC with the STK11 mutation, through targeted activation of the STING pathway by Mn-MSN@Met-M NPs. The proposed Mn-MSN@Met-M NPs, while structurally promising, require further validation concerning its long-term safety and efficacy in human subjects. Additionally, the study's findings are primarily based on the significant enhancement of T cells killing lung cancer H460 and LLC cells with the STK11 mutation *in vitro* and *in vivo*. These results might not extrapolate universally to other types of cells or mutations. Therefore, further studies on different types of cells and wider mutation ranges are necessitous to validate these findings.

STAR★METHODS

Detailed methods are provided in the online version of this paper and include the following:

- KEY RESOURCES TABLE
- RESOURCE AVAILABILITY
  - Lead contact
  - Materials availability
  - Data and code availability
- EXPERIMENTAL MODEL AND STUDY PARTICIPANT DETAILS
  - Ethics statement
  - Mice
- METHOD DETAILS
  - Synthesis of Mn-doped mesoporous silica NPs (Mn-MSNs)
  - In vitro drug release
  - Degradation experiment of Mn-MSN@Met-M Nps *in vitro* and Mn ions release assay
  - MRI assay *in vitro* and vivo
  - Cytotoxicity evaluation by CCK-8 assay
  - Homologous targeting assay
  - Cellular uptake and lysosomal escape *in vitro*
  - Cell viability assay
  - Colony formation assay
  - Western blotting assay detection of STING pathways
  - Enzyme-linked immunosorbent assay
  - *In vivo* biodistribution investigation
  - *In vivo* antitumor efficacy
- QUANTIFICATION AND STATISTICAL ANALYSIS

SUPPLEMENTAL INFORMATION

Supplemental information can be found online at https://doi.org/10.1016/j.isci.2024.110150.

ACKNOWLEDGMENTS

This work was financially supported by the Talent Cultivation Project of Army Medical University (No. 2022XQN46), National Natural Science Foundation of China (Grant No. 82172623), and Chongqing Technology Innovation and Application Development Special Key Project (No. CSTB2023TIAD-STX0003).

AUTHOR CONTRIBUTIONS

Y.D., J.Z., J.K., L.W., L.T., and Y.H. conceived and designed the experiments. Y.D., J.Z., J.K., L.W., D.H., Y.L., C.H., C.Lin, C.Lu, D.W., R.H., and L.L. performed the experiments. The manuscript was written by Y.D., J.Z., J.K., L.W., and Y.H.. L.T., and L.W. helped with study design and critically revised the manuscript. All authors discussed the results and reviewed the manuscript.

DECLARATION OF INTERESTS

The authors declare no competing interests.

Received: February 19, 2024
Revised: April 24, 2024
Accepted: May 28, 2024
Published: May 30, 2024

REFERENCES

1. Siegel, R.L., Miller, K.D., and Jemal, A. (2020). Cancer statistics, 2020. CA A Cancer J. Clin. *70*, 7–30. https://doi.org/10.3322/caac.21590.
2. Mathew, M., Enzler, T., Shu, C.A., and Rizvi, N.A. (2018). Combining chemotherapy with PD-1 blockade in NSCLC. Pharmacol. Ther. *186*, 130–137. https://doi.org/10.1016/j.pharmthera.2018.01.003.
3. Sanchez-Cespedes, M., Parrella, P., Esteller, M., Nomoto, S., Trink, B., Engles, J.M., Westra, W.H., Herman, J.G., and Sidransky, D. (2002). Inactivation of LKB1/STK11 is a common event in adenocarcinomas of the lung. Cancer Res. *62*, 3659–3662.
4. Kitajima, S., Ivanova, E., Guo, S., Yoshida, R., Campisi, M., Sundararaman, S.K., Tange, S., Mitsuishi, Y., Thai, T.C., Masuda, S., et al. (2019). Suppression of STING Associated with LKB1 Loss in KRAS-Driven Lung Cancer. Cancer Discov. *9*, 34–45. https://doi.org/10.1158/2159-8290.CD-18-0689.
5. Della Corte, C.M., and Byers, L.A. (2019). Evading the STING: LKB1 Loss Leads to STING Silencing and Immune Escape in KRAS-Mutant Lung Cancers. Cancer Discov. *9*, 16–18. https://doi.org/10.1158/2159-8290.CD-18-1286.
6. Zhou, C., Chen, X., Planells-Cases, R., Chu, J., Wang, L., Cao, L., Li, Z., López-Cayuqueo, K.I., Xie, Y., Ye, S., et al. (2020). Transfer of cGAMP into Bystander Cells via LRRC8 Volume-Regulated Anion Channels Augments STING-Mediated Interferon Responses and Anti-viral Immunity. Immunity *52*, 767–781.e6. https://doi.org/10.1016/j.immuni.2020.03.016.
7. Eikawa, S., Nishida, M., Mizukami, S., Yamazaki, C., Nakayama, E., and Udono, H. (2015). Immune-mediated antitumor effect by type 2 diabetes drug, metformin. Proc. Natl. Acad. Sci. USA *112*, 1809–1814. https://doi.org/10.1073/pnas.1417636112.
8. Kim, Y., Vagia, E., Viveiros, P., Kang, C.Y., Lee, J.Y., Gim, G., Cho, S., Choi, H., Kim, L., Park, I., et al. (2021). Overcoming acquired resistance to PD-1 inhibitor with the addition of metformin in small cell lung cancer (SCLC). Cancer Immunol. Immunother. *70*, 961–965. https://doi.org/10.1007/s00262-020-02703-8.
9. Xu, J., Liu, Y., Liu, S., Ou, W., White, A., Stewart, S., Tkaczuk, K.H.R., Ellis, L.M., Wan, J., Lu, X., and He, X. (2022). Metformin bicarbonate-mediated efficient RNAi for precise targeting of TP53 deficiency in colon and rectal cancers. Nano Today *43*, 101406. https://doi.org/10.1016/j.nantod.2022.101406.
10. Ren, D., Qin, G., Zhao, J., Sun, Y., Zhang, B., Li, D., Wang, B., Jin, X., and Wu, H. (2020). Metformin activates the STING/IRF3/IFN-β pathway by inhibiting AKT phosphorylation in pancreatic cancer. Am. J. Cancer Res. *10*, 2851–2864.
11. Huang, X., Sun, T., Wang, J., Hong, X., Chen, H., Yan, T., Zhou, C., Sun, D., Yang, C., Yu, T., et al. (2023). Metformin reprograms tryptophan metabolism to stimulate CD8+ T cell function in colorectal cancer. Cancer Res. *83*, 2358–2371. https://doi.org/10.1158/0008-5472.CAN-22-3042.
12. Finisguerra, V., Dvorakova, T., Formenti, M., Van Meerbeeck, P., Mignion, L., Gallez, B., and Van den Eynde, B.J. (2023). Metformin improves cancer immunotherapy by directly rescuing tumor-infiltrating CD8 T lymphocytes from hypoxia-induced immunosuppression. J. Immunother. Cancer *11*, e005719. https://doi.org/10.1136/jitc-2022-005719.
13. Wang, Z., Lu, C., Zhang, K., Lin, C., Wu, F., Tang, X., Wu, D., Dou, Y., Han, R., Wang, Y., et al. (2022). Metformin Combining PD-1 Inhibitor Enhanced Anti-Tumor Efficacy in STK11 Mutant Lung Cancer Through AXIN-1-Dependent Inhibition of STING Ubiquitination. Front. Mol. Biosci. *9*, 780200. https://doi.org/10.3389/fmolb.2022.780200.
14. Viveiros, P., Burns, M., Davis, A., Oh, M., Park, K., Jain, S., and Chae, Y.K. (2019). EP1.04-12 Response to Combination of Metformin and Nivolumab in a NSCLC Patient Whose Disease Previously Progressed on Nivolumab. J. Thorac. Oncol. *14*, S976. https://doi.org/10.1016/j.jtho.2019.08.2141.
15. Pietras, R., Xu, H., Hu, X., Matheny, C., Sandler, A., and Patel, M. (2018). P1.04-33 Retrospective Descriptive Analysis of Metformin with Atezolizumab in Advanced Non-Small Cell Lung Cancer in The OAK Trial. J. Thorac. Oncol. *13*, S538–S539. https://doi.org/10.1016/j.jtho.2018.08.748.
16. Li, L., Jiang, L., Wang, Y., Zhao, Y., Zhang, X.J., Wu, G., Zhou, X., Sun, J., Bai, J., Ren, B., et al. (2019). Combination of Metformin and Gefitinib as First-Line Therapy for Nondiabetic Advanced NSCLC Patients with EGFR Mutations: A Randomized, Double-Blind Phase II Trial. Clin. Cancer Res. *25*, 6967–6975. https://doi.org/10.1158/1078-0432.ccr-19-0437.
17. Pernicova, I., and Korbonits, M. (2014). Metformin—mode of action and clinical implications for diabetes and cancer. Nat. Rev. Endocrinol. *10*, 143–156. https://doi.org/10.1038/nrendo.2013.256.
18. Zhao, Z., Ma, Z., Wang, B., Guan, Y., Su, X.D., and Jiang, Z. (2020). Mn(2+) Directly Activates cGAS and Structural Analysis Suggests Mn(2+) Induces a Noncanonical Catalytic Synthesis of 2′3′-cGAMP. Cell Rep. *32*, 108053. https://doi.org/10.1016/j.celrep.2020.108053.
19. Lv, M., Chen, M., Zhang, R., Zhang, W., Wang, C., Zhang, Y., Wei, X., Guan, Y., Liu, J., Feng, K., et al. (2020). Manganese is critical for antitumor immune responses via cGAS-STING and improves the efficacy of clinical immunotherapy. Cell Res. *30*, 966–979. https://doi.org/10.1038/s41422-020-00395-4.
20. Song, Y., Liu, Y., Teo, H.Y., Hanafi, Z.B., Mei, Y., Zhu, Y., Chua, Y.L., Lv, M., Jiang, Z., and Liu, H. (2021). Manganese enhances the antitumor function of CD8(+) T cells by inducing type I interferon production. Cell. Mol. Immunol. *18*, 1571–1574. https://doi.org/10.1038/s41423-020-00524-4.
21. Chen, C., Tong, Y., Zheng, Y., Shi, Y., Chen, Z., Li, J., Liu, X., Zhang, D., and Yang, H. (2021). Cytosolic Delivery of Thiolated Mn-cGAMP Nanovaccine to Enhance the Antitumor Immune Responses. Small *17*, e2006970. https://doi.org/10.1002/smll.202006970.
22. Gao, M., Xie, Y.Q., Lei, K., Zhao, Y., Kurum, A., Van Herck, S., Guo, Y., Hu, X., and Tang, L. (2021). A Manganese Phosphate Nanocluster Activates the cGAS-STING Pathway for Enhanced Cancer Immunotherapy. Adv. Ther. *4*, 2100065. https://doi.org/10.1002/adtp.202100065.
23. Banala, V.T., Sharma, S., Barnwal, P., Urandur, S., Shukla, R.P., Ahmad, N., Mittapelly, N., Pandey, G., Dwivedi, M., Kalleti, N., et al. (2018). Synchronized Ratiometric Codelivery of Metformin and Topotecan through Engineered Nanocarrier Facilitates In Vivo Synergistic Precision Levels at Tumor Site. Adv. Healthcare Mater. *7*, e1800300. https://doi.org/10.1002/adhm.201800300.
24. Jia, L., Li, X., Liu, H., Xia, J., Shi, X., and Shen, M. (2021). Ultrasound-enhanced precision tumor theranostics using cell membrane-coated and pH-responsive nanoclusters assembled from ultrasmall iron oxide nanoparticles. Nano Today *36*, 101022. https://doi.org/10.1016/j.nantod.2020.101022.
25. Rao, L., Yu, G.T., Meng, Q.F., Bu, L.L., Tian, R., Lin, L.S., Deng, H., Yang, W., Zan, M., Ding, J., et al. (2019). Cancer Cell Membrane-Coated

Nanoparticles for Personalized Therapy in Patient-Derived Xenograft Models. Adv. Funct. Mater. *29*, 1905671. https://doi.org/10.1002/adfm.201905671.

26. Yu, L., Chen, Y., Wu, M., Cai, X., Yao, H., Zhang, L., Chen, H., and Shi, J. (2016). "Manganese Extraction" Strategy Enables Tumor-Sensitive Biodegradability and Theranostics of Nanoparticles. J. Am. Chem. Soc. *138*, 9881–9894. https://doi.org/10.1021/jacs.6b04299.
27. Hochmuth, R.M., Evans, C.A., Wiles, H.C., and McCown, J.T. (1983). Mechanical measurement of red cell membrane thickness. Science *220*, 101–102. https://doi.org/10.1126/science.6828875.
28. Tian, H., Luo, Z., Liu, L., Zheng, M., Chen, Z., Ma, A., Liang, R., Han, Z., Lu, C., and Cai, L. (2017). Cancer Cell Membrane-Biomimetic Oxygen Nanocarrier for Breaking Hypoxia-Induced Chemoresistance. Adv. Funct. Mater. *27*, 1703197. https://doi.org/10.1002/adfm.201703197.
29. Yang, G., Xu, L., Chao, Y., Xu, J., Sun, X., Wu, Y., Peng, R., and Liu, Z. (2017). Hollow MnO(2) as a tumor-microenvironment-responsive biodegradable nano-platform for combination therapy favoring antitumor immune responses. Nat. Commun. *8*, 902. https://doi.org/10.1038/s41467-017-01050-0.
30. Nesbitt, H.W., and Banerjee, D. (1998). Interpretation of XPS Mn(2p) spectra of Mn oxyhydroxides and constraints on the mechanism of MnO2 precipitation. Am. Mineral. *83*, 305–315. https://doi.org/10.2138/am-1998-3-414.
31. Liu, J., Chen, Q., Zhu, W., Yi, X., Yang, Y., Dong, Z., and Liu, Z. (2017). Nanoscale-Coordination-Polymer-Shelled Manganese Dioxide Composite Nanoparticles: A Multistage Redox/pH/H2O2-Responsive Cancer Theranostic Nanoplatform. Adv. Funct. Mater. *27*, 1605926. https://doi.org/10.1002/adfm.201605926.
32. Gu, Y., Lai, S., Dong, Y., Fu, H., Song, L., Chen, T., Duan, Y., and Zhang, Z. (2021). AZD9291 Resistance Reversal Activity of a pH-Sensitive Nanocarrier Dual-Loaded with Chloroquine and FGFR1 Inhibitor in NSCLC. Adv. Sci. *8*, 2002922. https://doi.org/10.1002/advs.202002922.
33. Varkouhi, A.K., Scholte, M., Storm, G., and Haisma, H.J. (2011). Endosomal escape pathways for delivery of biologicals. J. Contr. Release *151*, 220–228. https://doi.org/10.1016/j.jconrel.2010.11.004.
34. Hou, L., Tian, C., Yan, Y., Zhang, L., Zhang, H., and Zhang, Z. (2020). Manganese-Based Nanoactivator Optimizes Cancer Immunotherapy via Enhancing Innate Immunity. ACS Nano *14*, 3927–3940. https://doi.org/10.1021/acsnano.9b06111.
35. Ge, L., Qiao, C., Tang, Y., Zhang, X., and Jiang, X. (2021). Light-activated hypoxia-sensitive covalent organic framework for tandem-responsive drug delivery. Nano Lett. *21*, 3218–3224. https://doi.org/10.1021/acs.nanolett.1c00488.
36. Lin, S., Huang, G., Cheng, L., Li, Z., Xiao, Y., Deng, Q., Jiang, Y., Li, B., Lin, S., Wang, S., et al. (2018). Establishment of peripheral blood mononuclear cell-derived humanized lung cancer mouse models for studying efficacy of PD-L1/PD-1 targeted immunotherapy. mAbs *10*, 1301–1311. https://doi.org/10.1080/19420862.2018.1518948.
37. Koyama, S., Akbay, E.A., Li, Y.Y., Aref, A.R., Skoulidis, F., Herter-Sprie, G.S., Buczkowski, K.A., Liu, Y., Awad, M.M., Denning, W.L., et al. (2016). STK11/LKB1 Deficiency Promotes Neutrophil Recruitment and Proinflammatory Cytokine Production to Suppress T-cell Activity in the Lung Tumor Microenvironment. Cancer Res. *76*, 999–1008. https://doi.org/10.1158/0008-5472.CAN-15-1439.
38. Skoulidis, F., Goldberg, M.E., Greenawalt, D.M., Hellmann, M.D., Awad, M.M., Gainor, J.F., Schrock, A.B., Hartmaier, R.J., Trabucco, S.E., Gay, L., et al. (2018). STK11/LKB1 Mutations and PD-1 Inhibitor Resistance in KRAS-Mutant Lung Adenocarcinoma. Cancer Discov. *8*, 822–835. https://doi.org/10.1158/2159-8290.CD-18-0099.
39. Barber, G.N. (2015). STING: infection, inflammation and cancer. Nat. Rev. Immunol. *15*, 760–770. https://doi.org/10.1038/nri3921.
40. Zhu, Y., An, X., Zhang, X., Qiao, Y., Zheng, T., and Li, X. (2019). STING: a master regulator in the cancer-immunity cycle. Mol. Cancer *18*, 152. https://doi.org/10.1186/s12943-019-1087-y.
41. Pang, X., Fu, C., Chen, J., Su, M., Wei, R., Wang, Y., Lin, W., Wei, X., Jiang, X., Yang, X., et al. (2023). A manganese-phenolic network platform amplifying STING activation to potentiate MRI guided cancer chemo-/chemodynamic/immune therapy. Biomater. Sci. *11*, 3840–3850. https://doi.org/10.1039/d2bm02140d.
42. Mi, P. (2020). Stimuli-responsive nanocarriers for drug delivery, tumor imaging, therapy and theranostics. Theranostics *10*, 4557–4588. https://doi.org/10.7150/thno.38069.
43. Ma, G., Zhang, X., Zhao, K., Zhang, S., Ren, K., Mu, M., Wang, C., Wang, X., Liu, H., Dong, J., and Sun, X. (2024). Polydopamine Nanostructure-Enhanced Water Interaction with pH-Responsive Manganese Sulfide Nanoclusters for Tumor Magnetic Resonance Contrast Enhancement and Synergistic Ferroptosis–Photothermal Therapy. ACS Nano *18*, 3369–3381. https://doi.org/10.1021/acsnano.3c10249.
44. Dash, P., Piras, A.M., and Dash, M. (2020). Cell membrane coated nanocarriers - an efficient biomimetic platform for targeted therapy. J. Contr. Release *327*, 546–570. https://doi.org/10.1016/j.jconrel.2020.09.012.
45. Sun, X., Zhou, X., Lei, Y.L., and Moon, J.J. (2023). Unlocking the promise of systemic STING agonist for cancer immunotherapy. J. Contr. Release *357*, 417–421. https://doi.org/10.1016/j.jconrel.2023.03.047.
46. Gao, X., Wang, J., Wang, Y., Liu, S., Dong, K., Wu, J., Wu, X., Shi, D., Wang, F., and Guo, C. (2022). Fucoidan-ferulic acid nanoparticles alleviate cisplatin-induced acute kidney injury by inhibiting the cGAS-STING pathway. Int. J. Biol. Macromol. *223*, 1083–1093. https://doi.org/10.1016/j.ijbiomac.2022.11.062.
47. Gu, Y., Tang, J., Zhang, F., Qu, Y., Zhao, M., Li, M., Xie, Z., Wang, X., Song, L., Jiang, Z., et al. (2023). Manganese potentiates lipopolysaccharide-induced innate immune responses and septic shock. Int. J. Biol. Macromol. *230*, 123202. https://doi.org/10.1016/j.ijbiomac.2023.123202.
48. Gao, S., Lin, H., Zhang, H., Yao, H., Chen, Y., and Shi, J. (2019). Nanocatalytic Tumor Therapy by Biomimetic Dual Inorganic Nanozyme-Catalyzed Cascade Reaction. Adv. Sci. *6*, 1801733. https://doi.org/10.1002/advs.201801733.
49. Rao, L., Bu, L.-L., Cai, B., Xu, J.-H., Li, A., Zhang, W.-F., Sun, Z.-J., Guo, S.-S., Liu, W., Wang, T.-H., and Zhao, X.-Z. (2016). Cancer Cell Membrane-Coated Upconversion Nanoprobes for Highly Specific Tumor Imaging. Adv. Mater. *28*, 3460–3466. https://doi.org/10.1002/adma.201506086.
50. Liu, L., Bai, X., Martikainen, M.V., Kårlund, A., Roponen, M., Xu, W., Hu, G., Tasciotti, E., and Lehto, V.P. (2021). Cell membrane coating integrity affects the internalization mechanism of biomimetic nanoparticles. Nat. Commun. *12*, 5726. https://doi.org/10.1038/s41467-021-26052-x.

STAR★METHODS

KEY RESOURCES TABLE

REAGENT or RESOURCE	SOURCE	IDENTIFIER
Antibodies		
Rabbit anti-STING	CST	RRID:AB_2799375
Rabbit anti- Phospho-STING (Ser365)	CST	RRID:AB_2799831
Rabbit anti-TBK1	CST	RRID:AB_2255663
Rabbit anti-phospho (Ser172)-TBK1	CST	RRID:AB_10693472
Rabbit anti-IRF3	CST	RRID:AB_2722521
Rabbit anti-phospho(Ser379)-IRF3	CST	RRID:AB_2799943
Rabbit anti-β-Tubulin	CST	RRID:AB_823664
Rabbit anti-N-cadherin	Abcam	RRID:AB_1267002
Rabbit anti-EPCAM	Abcam	RRID:AB_732181
Rabbit anti-Galectin-3	Abcam	RRID:AB_1267156
Chemicals, peptides, and recombinant proteins		
Triethanolamine: TEA	Sigma-Aldrich	Cat#V900257
NaSal	Sigma-Aldrich	Cat#S3007
CTAB	Sigma-Aldrich	Cat#H5882
TEOS	Sigma-Aldrich	Cat#86578
Metformin	Sigma-Aldrich	Cat#317240
FITC	Sigma-Aldrich	Cat#46950
DMSO	Sigma-Aldrich	Cat#276855
$MnCl_2 \cdot 4H_2O$	Aladin	Cat#M112544
NH_4Cl	Aladin	Cat#A116364
$NH_3 \cdot H_2O$	Aladin	Cat#A112077
Pamoic acid	Aladin	Cat#P106763
Cy5 carboxylic acid	Aladin	Cat#C171352
Lyso-Tracker Red	Beyotime	Cat#C1046
DAPI	Beyotime	Cat#P0131
Crystal Violet Staining Solution	Beyotime	Cat#C0121
Critical commercial assays		
Cell Counting Kit-8	MedChemExpress	Cat#96992
BCA Protein Assay Kit	EMD Millipore	Cat#71285-3
PAGE Gel Silver Staining Kit	Solarbio	Cat#G7210
IFN-β ELISA Assay Kit	Finetest	Cat#EH0485
Experimental models: Cell lines		
NCI-H460	ATCC	Delf-10133
LLC Lewis	ATCC	Delf-10303
LLC STK11 mutation	Sino Biological Inc	http://www.blooge.com/
Human PBMCs	ATCC	Delf-12133
Experimental models: Organisms/strains		
NOD-SCID mice	Beijing Sibeifu Bioscience Co., Ltd	https://www.spfbiotech.com/

(*Continued on next page*)

Continued

REAGENT or RESOURCE	SOURCE	IDENTIFIER
Software and algorithms		
Origin 9.0 software	OriginLab Corporation	https://www.originlab.com/
ImageJ	Schneider et al.[7]	https://imagej.nih.gov/ij/
Other		
mini extrude	Avanti Polar Lipids	Cat#610000

RESOURCE AVAILABILITY

Lead contact

Further information and requests for resources and reagents should be directed to and will be fulfilled by the lead contact, Yong He, heyong@tmmu.edu.cn (lead contact).

Materials availability

All unique/stable reagents generated in this study are available from the lead contact with a completed Materials Transfer Agreement.

Data and code availability

- All data reported in this paper will be shared by the lead contact upon request.
- This paper does not report original code.
- Any additional information required to reanalyze the data reported in this paper is available from the lead contact upon request.

EXPERIMENTAL MODEL AND STUDY PARTICIPANT DETAILS

Ethics statement

Animal experiments were performed with the approval of the committee on animal experimentation of the Army Medical University (Chongqing, China. Approval number: SYXK(渝)2022-0003) and complied with all relevant ethical regulations (AMUWEC20210975).

Mice

To establish PBMCs-CDX mouse model,[36] H460 cells (5×10^5) were injected into the hind flanks of 6-8 weeks female NOD-SCID mice. The mice were subjected to tumor growth monitoring, and tumor volumes were calculated from caliper measurements using the following formula: (length ×width^2)/2. When tumors reached 80-100 mm^3 in volume, 5×10^6 human PBMCs were intravenously transplanted.

METHOD DETAILS

Synthesis of Mn-doped mesoporous silica NPs (Mn-MSNs)

Synthesis of mesoporous silica nanoparticles (MSN NPs)

MSN NPs were prepared as reported.[48] In a typical protocol, TEA (0.068 g) was diluted in pure water (25 mL) at 80°C under magnetic stirring for 0.5 h, followed by adding NaSal (84 mg) and CTAB (380 mg) (the CTAB/NaSal molar ratio is 0.5:1) to the reaction solution and keeping stirring for another 1 h. Then, TEOS (4 mL) was added dropwise into the reaction solution with gentle stirring for 2 h. The products were collected and washed several times with water and ethanol to remove the residual reactants.

Synthesis of Mn-doped mesoporous silica NPs (Mn-MSNs)

A mixture solution (10 mL) of $MnCl_2 \cdot 4H_2O$ (2 mg·mL^{-1}), NH_4Cl (10 mg·mL^{-1}) and $NH_3 \cdot H_2O$ (0.5 mL) was added into MSNs aqueous solution (10 mL, 1 mg·mL^{-1}). The mixture was transferred into an autoclave (50 mL) under hydrothermal treatment at 180°C for 10 h. The product was collected by centrifugation, and washed with water and ethanol for 3 times to remove the residual reactants completely.

Synthesis of Mn-MSN@Met NPs

The prepared Metformin (Met) loaded Mn-MSNs using the HIP Approach as previously reported method.[23] In brief, metformin at a concentration of 5 mg mL^{-1} was dissolved in phosphate buffered sucrose (PBS pH 9), which was mixed with Mn-MSNs to achieve a Met/Mn-MSN weight ratio of 1:1. Then, PA-DMSO (5.86 mg/m) was added rapidly into the reaction solution. After that, the mixture was incubated for 4 h at 60°C under ultrasonic concussion (50 Hz, 100 W). After incubation, drug-loaded particles were centrifuged at 10,000 rpm for 15 min, and washed with water for sever times to remove the residual reactants completely.

Preparation of cancer cell membrane-derived vesicles (M)

Cancer cell membrane-derived vesicles were prepared according to the previous report.[49] In details, to harvest membranes, cancer cells (H460 and LLC cells) were grown in T-175 culture flasks to full confluency and detached with 2 mM EDTA in PBS, and washed in PBS three times by centrifuging at 800 g for 5 min. The cells were suspended in hypotonic lysing buffer consisting of 20 mM Tris-HCl, 10 mM KCl, 2 mM $MgCl_2$, and 1 EDTA-free mini protease inhibitor tablet per 10 mL of solution and disrupted using a dounce homogenizer with a tightfitting pestle. The entire solution was subjected to 20 passes before spinning down at 3,200 g for 5 min. The supernatants were saved, while the pellet was resuspended in hypotonic lysing buffer and subjected to another 20 passes and spun down again. The supernatants were pooled and centrifuged at 20,000 g for 30 min, after which the pellet was discarded and the supernatant was centrifuged again at 80,000 g for 1.5 h using an ultra-speed centrifuge (LE-80K, Beckman Coulter, USA). The pellet containing the plasma membrane material was then washed once with 10 mM Tris-HCl and 1 mM EDTA. The final pellet was collected as purified cancer cell membranes, and then cancer cell membrane-derived vesicles were obtained by physically extruding the pellet for 11 passes through a 400 nm polycarbonate porous membrane on a mini extruder (Avanti Polar Lipids, USA).

Preparation of Mn-MSN@Met-M

To coat cancer cell membranes onto the Mn-MSN@Met NPs, 1 mL PBS containing 100 μg Mn-MSN@Met NPs was mixed with the prepared cancer cell membrane-derived vesicles, the mass ratio of Mn-MSN@Met NPs to cancer cell membranes was 1:5.[50] The mixture was subsequently extruded 11 times through 200 nm pores and then centrifuged at 1,000 g to remove excess vesicles. Finally, the resulting cancer cell membrane-cloaked particles (Mn-MSN@Met-M) were left in PBS overnight at 4°C for further use.

Characterization of Mn-MSN@Met-M NPs

The hydrodynamic diameter and zeta potential were measured by a dynamic light scatter (DLS; Nano-Zen 3600, Malvern Instruments, UK). The morphology of Mn-MSNs, Mn-MSN@Met and Mn-MSN@Met-M were characterized using a Scanning electron microscopy (SEM) (FIB-SEM microscope, Crossbeam 340, Zeiss) and transmission electron microscope (TEM; JEM-2010 ES500W, Japan). Energy dispersive X-ray spectroscopy (EDS) was performed simultaneously on JEM-2100F electron microscope. The N_2 adsorption-desorption isotherm and corresponding pore-size distribution were tested to characterize the mesoporous structure of NPs by a Micrometitics Tristar 3000 system (Norcross, GA). The phases of NPs were measured by X-ray diffraction (XRD Bruker D8 Focus, Germany) with a monochromatized source of Cu Ka1 radiation (l = 0.15405 nm) at 1.6 kW (40 kV, 40 mA). X-ray photoelectron spectroscopy (XPS) was acquired to observe the different valence states of doped manganese component on an ESCALAB 250Xi X-ray photoelectron spectroscopy. UV-visible spectroscopy was conducted on an ultraviolet spectrophotometer (TU-1901, Beijing Purkinje General instrument, China). The membrane-associated proteins of Mn-MSN@Met-M NPs were detected by sodium dodecyl sulfate-polyacrylamide gel electrophoresis (SDS-PAGE), and stain by silver stain kit to visualize the protein bands. The cellular adhesion molecules (e.g., epithelial cell adhesion molecule (EpCAM), Galectin-3, and N-cadherin) of Mn-MSN@Met-M NPs were analyzed by western blot (WB).

In vitro drug release

Mn-MSN@Met-M NPs (1 mg) was dispersed into PBS buffer at various GSH concentrations (0/5 mM) or pH (pH: 7.4/5.5) , respectively. At given time points, 500 μL of solution was extracted and characterized by a UV-vis spectrophotometer at a wavelength of 237 nm (metformin) after centrifuging.

Degradation experiment of Mn-MSN@Met-M Nps *in vitro* and Mn ions release assay

In vitro degradation profiles and microstructure evolutions of Mn-MSN@Met-M NPs were assessed by two typical approaches. One was detecting the degradation content of Mn by inductively coupled plasma mass spectrometry (ICP-MS, 7800 ICP-MS, Agilent), and the other was directly observing the time-dependent structural evolution of Mn-MSN@Met-M NPs by SEM during the degradation evaluation. Typically, Mn-MSN@Met-M was added into PBS buffer at various GSH concentrations (0/5 mM) or pH (pH: 7.4/5.5), respectively. It was noted that all the evaluation was based on the concentration of 1.0 mg/mL Mn-MSN@Met-M. The testing solution was put into a water bath at 37°C under magnetic stirring slowly (250 rpm). At given time, a small amount of degradation solution was taken out for ICP-MS test and SEM observation.

MRI assay *in vitro* and vivo

The *in vitro* MR imaging experiments were performed on a 3.0 T clinical MRI instrument (GE Signa LX 3.0 T). The manganese concentrations of Mn-MSN@Met-M NPs dispersed in PBS buffer at various GSH concentrations (0/5 mM) or pH (pH: 7.4/5.5) were determined by ICP-MS after incubation 24 h. T_1-weighted Fast-recovery spin-echo (FR-FSE) sequence is described as follows: TR=1000, 2000, 3000 and 4000, Slice=3mm, Space=0.5 mm, Fov=20, Phase fov=0.8, Freq x Phase=384 x 256, Nex=2, ETL= 2.

In vivo T1-weighted MRI images of H460 cell tumor-bearing mice treated with Mn-MSN@Met-M NPs (24.8 mg/kg of Mn-MSN@Met-M NPs) at different time points after injection.

Cytotoxicity evaluation by CCK-8 assay

H460 and LLC cell were cultured in 96-well plates at a density of 1.0×10^4 cells per well in 100 μL DMEM containing 10% (v/v) FBS, 100 U/mL of penicillin, and 100 mg/mL of streptomycin. Cells were incubated at 37°C in a humidified atmosphere containing 5% CO_2 before additional experiments. After 24 h, cells were treated with Mn-MSN@Met or Mn-MSN@Met-M (from 0.01, 0.02, 0.05, 0.1, 0.2, 0.5, 1.0 to 2.0 mg/mL). The cell viability was quantified by CCK-8 assay (MCE, USA).

Homologous targeting assay

Cy5-labeled Mn-MSN@Met NPs was first prepared by mixing Cyanine 5 carboxylic acid (J&K, China) with Mn-MSN@Met NPs for 24 h and then centrifuging to remove excess Cy5. Then, H460 and LLC cells were seeded in 6-well plate at a density of 10^6 cells per dish and cultured for 12 h, and the growth medium was removed. Then cell culture media containing 100 μg mL^{-1} nanoparticles (i.e., free Cy5, Cy5-labeled Mn-MSN@Met NPs, H460 membrane coated Cy5-labeled Mn-MSN@Met NPs, and LLC membrane coated Cy5-labeled Mn-MSN@Met NPs was added in. Subsequently, the cells were incubated for 4 h, washed with PBS, stained with 4′,6-diamidino-2-phenylindole (DAPI), washed once again, fixed with 4% paraformaldehyde (PFA) at room temperature, and finally imaged by using a fluorescence microscope (Leica DM2500, Germany). Flow cytometry was also employed to measure the capability of nanoparticles targeting to H460 or LLC cells. After incubated with nanoparticles as described above, the cells were digested and DAPI stained. Finally, the obtained samples were run on a flow cytometer (FACScaliber, Becton Dickinson, USA) and the data was analyzed by using the FlowJo Software (Tree Star, USA).

Cellular uptake and lysosomal escape *in vitro*

To investigate the cellular uptake of Mn-MSN@Met NPs, H460 cells were seeded in Confocal Dishes with the cell density of 2.5×10^5 cells per well and cultured for 24 h at 37°C. Thereafter, the free Cy5 (Simulate small molecule drugs) and Cy5-labed Mn-MSN@Met NPs were receptively added to the dishes separately and further incubated for 4 h. Afterward, the cells were washed with PBS for three times and then fixed with 4% paraformaldehyde for 15 min at room temperature. Then, the lysosomal and nucleus was stained by lysosomal green and DAPI (Beyotime, Shanghai, China) receptively, and imaged by confocal laser scanning microscopy (Olympus, Japan, FV1000).

Cell viability assay

CCK-8 assay was used to evaluate the killing effects of T cells enhanced by Mn-MSN@Met NPs on H460 and LLC cells. Briefly, the H460 or LLC were seeded in 96-well plates at a density of 1×10^4 cells per well and cultured for 12 h. The above cells were treated with specific concentrations of Mn-MSN-M, metformin, and Mn-MSN@Met-M nanoparticles in combination with different proportions of T lymphocytes and tumor cells (cancer cell/T cell 1:0, 1:0.1, 1:0.2, 1:0.5, 1:1, 1:2, 1:5, 1:10), and incubated at 37°C for 72 h. Cells grown without any particles were used as a control. At the end of the incubation, CCK-8 was added to test the cell viability.

Colony formation assay

The H460 and LLC cells were seeded in 6-well plate at a density of 300 cells/well. After 12 h, The above cells were treated with specific concentrations of Mn-MSN-M, metformin, and Mn-MSN@Met-M nanoparticles in combination with different proportions of T lymphocytes and tumor cells (cancer cell/T cell 1:0, 1:0.1, 1:0.2, 1:0.5, 1:1, 1:2, 1:5, 1:10). After 15 days of exposure, the cells were washed with PBS and fixed with 4% paraformaldehyde for 15 min at room temperature. Then, the cells were stained for 30 min with crystal violet solution. Colonies were manually scored under a stereomicroscope.

Western blotting assay detection of STING pathways

After H460 and LLC cells were incubated with the medium containing different nanoparticles (Mn-MSN-M, metformin, Mn-MSN@Met-M NPs) for 72 h, the cell samples were obtained. A western blotting assay was used to characterize the expression of STING/p-STING, TBK1/p-TBK1, IRF3/p-IRF3.

Enzyme-linked immunosorbent assay

IFN-β levels were measured by ELISA assay (Finetest, Wuhan, China). Briefly, After H460 cells were incubated with the medium containing different nanoparticles (Mn-MSN-M, metformin, Mn-MSN@Met-M NPs) for 72 h, the medium supernatant were collected and assayed according to the manufacturer's instructions. Values represent the average of three replicates from at least three independent experiments.

In vivo biodistribution investigation

When tumors were increased to ~150-200 mm^3 in volume, the mice were randomly divided into four groups. Then, the free Cy5, Mn-MSN@Met-M, and Cy5-labeled Mn-MSN@Met-M NPs were i.v. injected into the tumor bearing mice, and the fluorescence images were recorded by IVIS (Biolight Biotechnology, Antview, china) at 24 h after the injection. Then, the mice were sacrificed, and the major organs (heart, liver, spleen, lung, and kidney) and tumor tissues were collected for further *ex vivo* image.

In vivo antitumor efficacy

When tumors were increased to ~150-200 mm^3 in volume, the mice were randomly divided into eight groups, and each group involved five mice. H460 tumor-bearing mice were treated with different nanocomposites by intravenous injection for 28 days at the dose of 5 mg kg^{-1} per mouse $(3\ day)^{-1}$. Each mouse was earmarked and followed individually throughout the whole experiment. The tumor volume and body weight were then determined according to the method as described above every 3 days for 4 weeks until the euthanasia. They were treated as follows: Group 1, intravenous injection of 0.9% NaCl; Group 2, PD-1 inhibitor (Pembrolizumab, 25 mg/kg) was injected every 3 days intraperitoneally; Group 3, Metformin (1 mg/ml) was dissolved in drinking water and given to mice orally; Group 4, PD-1 inhibitor (Pembrolizumab, 25 mg/kg) injected plus Metformin (1 mg/ml) oral; Group 5, intravenous injection of the Mn-MSN-M; Group 6, intravenous injection of the Mn-MSN-M and PD-1 inhibitor (Pembrolizumab, 25 mg/kg); Group 7, intravenous injection of the Mn-MSN@Met-M; Group 8, intravenous injection of the Mn-MSN@Met-M and PD-1 inhibitor (Pembrolizumab, 25 mg/kg). Tumor growth was monitored every 3 days. Cohorts were sacrificed when control mice tumors reached 15 mm in any direction measured. The therapeutic effects were evaluated by monitoring the changes of relative body weight and relative tumor volume of the mice in different groups. Finally, the mice were sacrificed, and the tumor tissues were collected for further analysis the Mn ions and metformin concentrations by ICP-AES and LC-MS (Agilent 1290II-6460, USA) respectively. Finally, the mice were sacrificed, and the major organs and tumor tissues were collected for further analysis of H&E.

QUANTIFICATION AND STATISTICAL ANALYSIS

All data are expressed as mean $\pm$ SD and the statistical analysis was performed by Origin 9.0 software (OriginLab Corporation, Northampton, MA). Differences between two groups were analyzed by Student'sttest. A p value <0.05 was considered statistically significant.